# Growth behaviors and emission properties of Co-deposited $MAPbI_3$ ultrathin films on $MoS_2$

Siwen You(游思雯)[1], Ziyi Shao(邵子依)[1], Xiao Guo(郭晓)[1], Junjie Jiang(蒋俊杰)[1], Jinxin Liu(刘金鑫)[1], Kai Wang(王凯)[1], Mingjun Li(李明君)[1], Fangping Ouyang(欧阳方平)[1], Chuyun Deng(邓楚芸)[2], Fei Song(宋飞)[3], Jiatao Sun(孙家涛)[4], and Han Huang(黄寒)[1,†]

[1] *Hunan Key Laboratory of Super-Microstructure and Ultrafast Process, School of Physics and Electronics, Central South University, Changsha* 410083, *China*
[2] *College of Arts and Science, National University of Defense Technology, Changsha* 410073, *China*
[3] *Key Laboratory of Interfacial Physics and Technology, Shanghai Institute of Applied Physics, Chinese Academy of Sciences, Shanghai* 201000, *China*
[4] *School of Information and Electronics, MIIT Key Laboratory for Low-Dimensional Quantum Structure and Devices, Beijing Institute of Technology, Beijing* 100081, *China*

(Received 24 June 2022; revised manuscript received 15 August 2022; accepted manuscript online 2 September 2022)

Hybrid organic–inorganic perovskite thin films have attracted much attention in optoelectronic and information fields because of their intriguing properties. Due to quantum confinement effects, ultrathin films in nm scale usually show special properties. Here, we report on the growth of methylammonium lead iodide ($MAPbI_3$) ultrathin films via co-deposition of $PbI_2$ and $CH_3NH_3I$ (MAI) on chemical-vapor-deposition-grown monolayer $MoS_2$ as well as the corresponding photoluminescence (PL) properties at different growing stages. Atomic force microscopy and scanning electron microscopy measurements reveal the $MoS_2$ tuned growth of $MAPbI_3$ in a Stranski–Krastanov mode. PL and Kelvin probe force microscopy results confirm that $MAPbI_3/MoS_2$ heterostructures have a type-Ⅱ energy level alignment at the interface. Temperature-dependent PL measurements on layered $MAPbI_3$ (at the initial stage) and on $MAPbI_3$ crystals in averaged size of 500 nm (at the later stage) show rather different temperature dependence as well as the phase transitions from tetragonal to orthorhombic at 120 and 150 K, respectively. Our findings are useful in fabricating $MAPbI_3$/transition-metal dichalcogenide based innovative devices for wider optoelectronic applications.

**Keywords:** $MAPbI_3/MoS_2$ heterostructure, Co-deposition, temperature-dependent photoluminescence, growth behavior

**PACS:** 79.60.Jv, 63.20.kd, 78.55.–m, 64.70.Nd **DOI:** 10.1088/1674-1056/ac8e9b

## 1. Introduction

Perovskites (PVKs) have raised much attention in semiconductor applications, such as solar cells, light emitting diodes, and photodetectors, due to their exceptional optoelectronic properties.[1–5] Among them, $MAPbI_3$ is a representative one due to its simple structure, suitable bandgap for solar absorption, and long-range balanced electron–hole transport lengths.[6,7] Properties of elementary excitation of $MAPbI_3$, such as the values of exciton binding energy and the strength of electron-phonon coupling, are essential for development of high-efficiency devices. According to the temperature dependence of integrated intensity of the photoluminescence (PL) emission peak, the exciton binding energy of $MAPbI_3$ has been extracted to be 15–60 meV,[8–10] which is so small that separation and migration of electrons and holes in $MAPbI_3$ thin films (300 nm) can be facilitated. Electron–phonon coupling sets a basic intrinsic limit to charge carrier mobility in non-intrinsic scattering without impurities and has been proved to generate homogeneous emission linewidth broadening in semiconductors.[11] Especially, it has comparable effects on temperature-induced renormalization of bandgap with thermal expansion in $MAPbI_3$ bulk or thin films, but enhanced contribution in $MAPbI_3$ nanocrystals in size of several nanometers because of the strong quantum confinement effects.[12]

Accompanied with the miniaturization of devices, the functional material films become thinner and thinner. $MAPbI_3$ thin films prepared by the solution spin coating method are usually several hundreds of nm in thickness and their properties are close to their bulk counterparts.[13] Methylammonium lead tribromide nanocrystals in different sizes (1.5–3 nm) formed in metal oxide porous scaffolds show a wavelength-tunable emission from green to blue due to the quantum confinement effects.[14] Highquality $MAPbI_3$ nanosheets as thin as 1.3 nm have been fabricated by converting solution-processed $PbI_2$ in MAI vapor, but the preparation process and their thicknesses are not controllable.[15] Transition-metal dichalcogenides (TMDCs) are good templates to realize van der Waals epitaxial growth of $MAPbI_3$ due to the dangling bond-free surfaces.[16–19] In previous reports, thickness-controllable $MAPbI_3$ ultrathin layers are successfully fabricated on chemical vapor deposition (CVD)-grown or mechanical exfoliation monolayer TMDCs using a two-step sequential deposition method.[20,21] However, such a method has some shortcomings, such as the volume expansion and structure damage in MAI intercalation process. The Co-deposition

[†]Corresponding author. E-mail: physhh@csu.edu.cn
© 2023 Chinese Physical Society and IOP Publishing Ltd

method is superior for preparing $MAPbI_3$ thin films with a wide range of clean interfaces, homogeneous morphology, and better stability.[22–25] However, it is still of challenge to prepare and investigate properties of ultrathin $MAPbI_3$ thin films with high quality.

In this work, we systematically investigate the growth behaviors of $MAPbI_3$ films via co-deposition of $PbI_2$ and MAI on CVD-grown monolayer $MoS_2$ as well as the corresponding photoluminescence properties and emission behaviors at different growing stages using atomic force microscopy (AFM), scanning electron microscopy (SEM), PL, and Kelvin probe force microscopy (KPFM) measurements. Temperature-dependent PL measurements reveal thickness-dependent trends of emission photon energy in $MAPbI_3/MoS_2$ heterostructures from 300 K to 80 K.

## 2. Experimental methods

Monolayer $MoS_2$ was prepared by the conventional CVD method with two temperature zone systems on the c-sapphire substrate. S (aladdin 99.999%) and $MoO_3$ (aladdin 99.99%) powders were used as precursors, as well as nitrogen ($N_2$) carries the reactants as an inert gas.[26,27] A previously reported co-deposition method was adopted to fabricate $MAPbI_3$ ultrathin films on c-sapphire substrates partially covered with monolayer $MoS_2$ in a high-vacuum system with base pressure better than $5.0\times10^{-5}$ Pa.[22,28] There are two temperature-controlled K-cells at the bottom of the system, loaded with the precursor materials of $PbI_2$ (aldrich, 98+%) and MAI (polymer, 99.5%), respectively. The deposition temperatures of $PbI_2$ and MAI are 573 K and 415 K, respectively, and the deposition rates of the precursor at 6 Å/min for $PbI_2$ and 15 Å/min for MAI are monitored by quartz crystal microbalance. The deposition times are 2 min, 4 min, and 6 min. The corresponding samples with a nominal thickness $\sim$ 2 nm, 4 nm, and 8 nm are named as samples I, II, and III, respectively.

AFM measurements were carried out in a tapping mode (Agilent 5500, USA).[29] SEM was obtained with an MIRA3 LMH (TESCAN Chech) field emission scanning electron microscope. PL spectra were collected in a confocal Raman microscope system (Renishaw inVia Qontor, UK) using a 532 nm laser and 1800 lines/mm grating, where a sample stage (THMS 600) with the temperature varying from 78 K to 873 K is equipped.[30,31] All spectra were taken at laser power density 1 mW/μm$^2$ for 1 s and were fitted by Gaussian and Lorentzian mixed deconvolution. X-ray diffraction (XRD) patterns were measured by a PANalytical Empyren system with Cu $K_\alpha$ radiation ($\lambda = 0.154$ nm). KPFM images were recorded using an NTEGRA spectra system (NT-MDT, Russia).

## 3. Results and discussion

Figure 1(a) shows a typical AFM image of a triangular CVD-grown $MoS_2$ flake, whose thickness is $\sim$ 0.9 nm, as shown in the profile along the red line, indicating a monolayer $MoS_2$.[32] Upon 2 nm $MAPbI_3$ deposition (sample I), dispersed bright protrusions with a height up to 8 nm appeared on the bare c-sapphire surface, as shown in Fig. 1(b). On the contrary, the $MoS_2$ flake appears as atomically smooth as the pristine one except for some features on its edges. The corresponding line profile displays that the thickness in the triangular $MoS_2$ region is almost doubled ($\sim$ 1.6 nm), and the dim features have an additional height of $\sim$ 0.8 nm, indicating that a monolayer $MAPbI_3$ is grown on $MoS_2$, and new nuclei start at the edges. Upon 4-nm $MAPbI_3$ deposition (sample II), the bright protrusions on c-sapphire (region B) became denser and higher ($\sim$ 30 nm) as shown in Fig. 1(c), indicating a nucleation-limited growth. The triangular $MoS_2$ region (region A) has no apparent change except that its thickness increases to 4 nm. We speculate that at the beginning, $MAPbI_3$ grows in a Frank–van der Merwe mode on $MoS_2$ and in a Volmer–Weber mode on c-sapphire. Different growth behaviors of $MAPbI_3$ on two substrates may be attributed to their different hydrophilicity and lower nucleation energy on $MoS_2$.[16,33] Therefore, $MoS_2$ is a good template to realize van der Waals epitaxial growth of $MAPbI_3$ due to the dangling bondfree surface. Upon 8-nm $MAPbI_3$ deposition (sample III), although the triangular shape of $MoS_2$ is still observable, the entire surface is covered by clusters (up to 60 nm high) as shown in Fig. 1(d), indicating that the growth mode of $MAPbI_3$ on $MoS_2$ changes to the Stranski–Krastanov (S-K) mode. It reveals the limited influence of $MoS_2$ on the growth of $MAPbI_3$. The SEM image in Fig. 1(e) shows the grainy features in more details than the AFM image due to no tip effect. The averaged grain size of $MAPbI_3$ on $MoS_2$ ($\sim$ 500 nm) is larger than that on the c-sapphire substrate ($\sim$ 200 nm) because the dangling-bond-free surface of $MoS_2$ could motivate the migration of atoms precursor molecules (MAI and $PbI_2$) and promote the growth of $MAPbI_3$ grains, which is in agreement with the previous reports.[16,17] The corresponding XRD pattern in Fig. 1(e) shows the peaks at 14.2°, 28.3°, and 33.1°, assigned to the (110), (220), and (310) planes of crystalline $MAPbI_3$ in the tetragonal phase, respectively.[34] The grain dimension in the perpendicular direction is estimated to be $\sim$ 33 nm according to the Scherrer equation. No $PbI_2$ related peaks can be detected, confirming the high quality of the prepared sample. Figure 1(f) schematically demonstrates the growth modes of $MAPbI_3$ on $MoS_2$. The x-ray photoelectron spectra (XPS) full spectra of samples are shown in Fig. S1 in the supporting information, where Pb, I, N, and C elements are detected. In the future, atomically resolved methods like high resolution transmission electron microscopy (HRTEM) and scanning tunneling microscopy (STM) can be used to investigate the detailed structure or the quality of $MAPbI_3/MoS_2$ heterostructures.

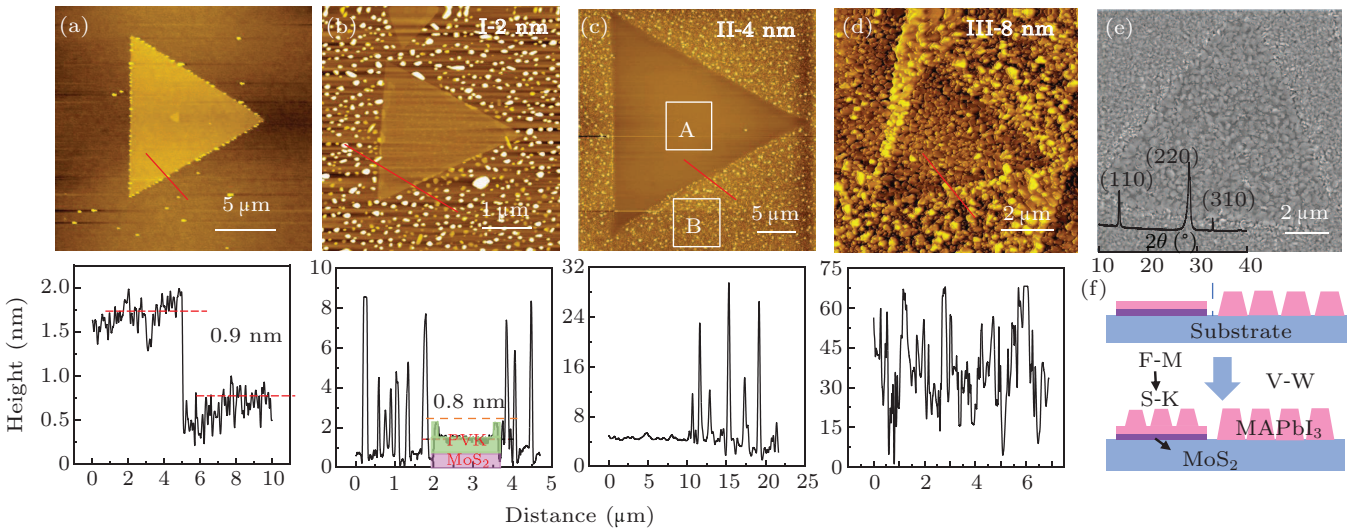



**Fig. 1.** Typical AFM images of CVD-grown $MoS_2$ on c-sapphire (a), and co-deposited $MAPbI_3$ ultrathin films in various nominal thicknesses [(b) 2 nm, (c) 4 nm, (d) 8 nm)] on top, named as sample I, Ⅱ, and Ⅲ. The corresponding scan profiles are given. (e) Representative SEM image of 8-nm-thick $MAPbI_3$ (sample-Ⅲ). The corresponding XRD pattern is inserted. (f) Schematic illustration of different growth modes of $MAPbI_3$ on c-sapphire with and without $MoS_2$.

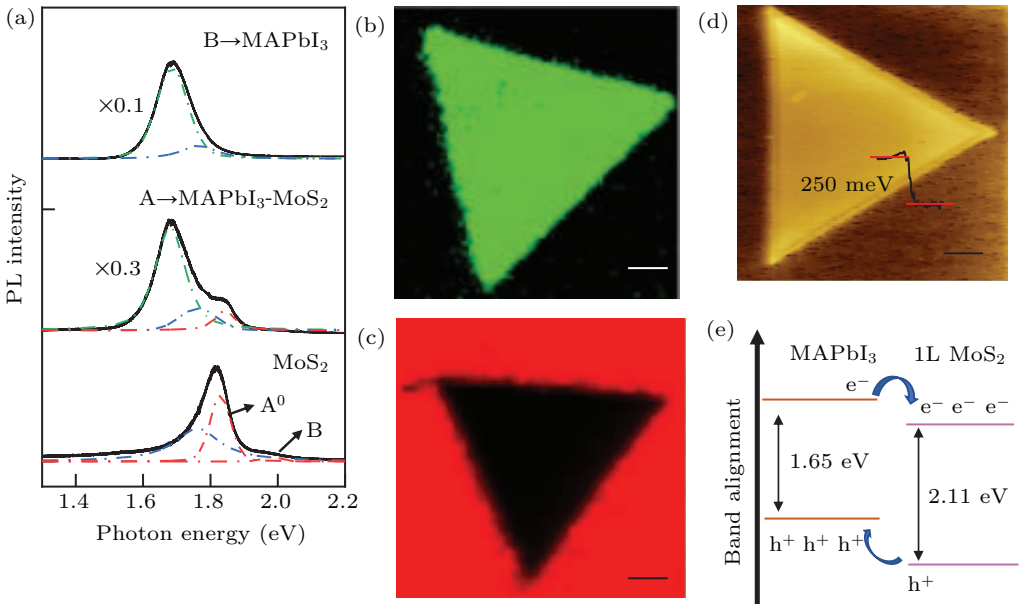



**Fig. 2.** Characterizations of $MAPbI_3/MoS_2$ heterostructure (sample Ⅱ): (a) PL spectra collected from CVD-grown $MoS_2$, $MAPbI_3$ on c-sapphire with and without $MoS_2$ regions, (b) PL mapping of a CVD-grown $MoS_2$ flake, (c) PL mapping and (d) KPFM image of the $MAPbI_3/MoS_2$ heterostructure. Scale bar: 5 μm. (e) Schematic illustration of the type-Ⅱ energy level alignment of $MAPbI_3/MoS_2$ heterostructure.

PL measurements were performed to investigate the optical properties of sample Ⅱ, as shown in Fig. 2(a). The peak intensities were normalized by the bottom panel. The PL spectrum of CVD-grown $MoS_2$ exhibits three peaks (fitted) at 1.76 eV, 1.84 eV, and 1.99 eV, corresponding to the free exciton of c-sapphire substrate (blue plot), exciton A and exciton B of $MoS_2$ (red plot), respectively. The better distribution and uniformity of $MoS_2$ can be reflected by the PL mapping of exciton A, as shown in Fig. 2(b). For sample Ⅱ, two representative PL spectra from regions A and B are shown in Fig. 2(a). Besides the original emission peaks of $MoS_2$ and sapphire, an additional emission peak centered at 1.68 eV with a full width at half maximum (FWHM) of 0.11 eV can be observed, which belongs to the $MAPbI_3$ (green plot). It is worth noting that the emission peak intensity of $MoS_2$ is higher than that of sapphire without $MAPbI_3$, while they are almost equal after deposition of $MAPbI_3$, revealing the quenching of $MoS_2$ emission peak intensity. Moreover, the PL intensity of $MAPbI_3$ on $MoS_2$ (region A) is quenched by a factor of 3 times compared to that on c-sapphire (region B). As shown in Fig. 2(c), the PL intensity mapping at 1.68 eV was measured. It was observed that the PL intensity in region A was significantly lower than that in region B, indicating the PL quenching of $MAPbI_3$ on $MoS_2$. For sample Ⅲ, the PL emission peak of $MAPbI_3$ is located at 1.64 eV and there is no $MoS_2$ signal anymore because of strong luminescence properties of thicker $MAPbI_3$, as shown in Fig. S2(a). The clear redshift of the emission peak can be ascribed to the thickness-dependent quantum confinement ef-

fect of $MAPbI_3$ layer.[20] Moreover, the intensity of emission peak is still quenched in the heterostructure.

To further investigate the surface charge distribution in heterostructures, KPFM measurements were carried out. The contact potential difference (CPD) is defined as the work function difference between the sample surface and the cantilever tip. As shown in Fig. 2(d), the CPD difference between $MAPbI_3/MoS_2$ and pure $MAPbI_3$ regions is determined to be about 250 mV, which indicates that the work function of pure $MAPbI_3$ is 250 meV smaller than that of $MAPbI_3/MoS_2$. It reveals the formation of electric dipoles pointing out of the plane in the $MAPbI_3/MoS_2$ heterostructure region, due to the interfacial electron transfer from $MAPbI_3$ into $MoS_2$, resulting in separation of holes and electrons distributions on two sides.[18,35,36] Taking the PL quenching at the heterostructure interface into consideration, we can get a conclusion that a representative type-Ⅱ band alignment of $MAPbI_3/MoS_2$ heterostructure is formed as shown in Fig. 2(e), which is in agreement with the previous reports.[17,21,37,38] Taking the transport gaps of $MAPbI_3$ and monolayer $MoS_2$ as 1.65 eV and 2.11 eV,[39] respectively, both conduction band minimum (CBM) and valence band maximum (VBM) levels of $MAPbI_3$ are higher than those of $MoS_2$.[40,41] For sample Ⅲ, the CPD difference is $\sim$ 20 mV [see Fig. S2(b)], which may be attributed to the different morphologies of the heterostructures. The work function of $MAPbI_3$ changes as the surface becomes rougher. Profiting from the effective interfacial charge carrier separation in ultrathin type-Ⅱ $MAPbI_3/MoS_2$ heterostructure, they are excellent candidates for designing high-performance photodetector devices.

To better understand the thickness-dependent photophysical properties of $MAPbI_3/MoS_2$, temperature-dependent PL measurements from 300 K to 80 K are carried out. Figure 3(a) shows the temperature evolutions of PL spectra of sample Ⅲ. There is a dominant and symmetric emission peak located at around 1.64 eV (peak I), belonging to the tetragonal-I phase ($I4/mcm$ group) $MAPbI_3$.[9] Below 150 K, a new emission peak appears at 1.69 eV (peak Ⅱ), arising from the orthorhombic phase $MAPbI_3$. These emission peaks of tetragonal and orthorhombic phase are ascribed to the free exciton recombination.[41] The atomic models of tetragonal and orthorhombic phases are shown in the insets of Fig. 3(a).[42] In order to understand the evolution of fitting emission peak, PL spectra at six representative temperatures are shown in Fig. S3. As the temperature decreases to 100 K, a new-emerging emission component occurs at the low-energy side centered at 1.56 eV (peak Ⅲ), which can be attributed to the trap-mediated exciton radiative recombination.[43] Figure 3(b) shows the photon energy evolution of the fitted three emission peaks of $MAPbI_3$ with temperature according to the experimental spectra. Peak I has a redshift from 1.64 eV to 1.59 eV in the temperature range from 300 K to 150 K. This trend is consistent with the previous report on pure $MAPbI_3$.[9] The phase transition from tetragonal to orthorhombic for such $MAPbI_3/MoS_2$ starts to take place at 150 K, which is higher than that for pure $MAPbI_3$ ($\sim$ 120 K), close to that of bulk.[12] From 150 K to 100 K, peak I (tetragonal) displays a slight blueshift while peak Ⅱ (orthorhombic) keeps the trend of redshift. According to the integrated intensity of the fitted three emission peaks, the relative percentage evolution as a function of temperature is shown in Fig. 3(c). As the temperature decreases, the ratio of the tetragonal phase goes down continuously while that of orthorhombic increases. It is worth noting that the ratio of trapped exciton peak keeps growing at low temperatures, attributed to the smaller binding energy of trapped excitons and surface state transitions.[41]

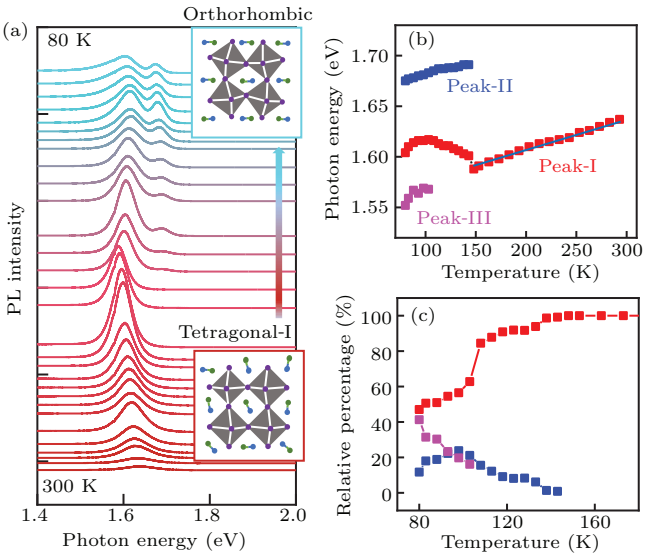



**Fig. 3.** Optical transition properties of sample Ⅲ in the temperature range of 300–80 K. (a) Temperature-dependent PL spectra. (b) Experimental data and fitting curve of photon energy as a function of temperature. Red: tetragonal phase. Blue: orthorhombic phase. Purple: the defect peak. (c) Relative percentage of three peaks in $MAPbI_3/MoS_2$ heterostructure.

For $MAPbI_3$ on $MoS_2$ in sample Ⅱ (region A), the evolution of PL spectra as a function of temperature looks rather different, as shown in Fig. 4(a). The intensity of the main peak located at 1.68 eV (peak Ⅳ) increases as the temperature decreases from 300 K to 120 K. It results from the enhanced optical matrix elements on account of the reinforced Coulomb attraction, and is a representative behavior of free-exciton radiative recombination.[41] Although the PL signal of $MoS_2$ is weak, a blueshift of photon energy is still observable, consistent with the trend of traditional semiconductors.[44] See Fig. S4 for more details. No trapped exciton peak can be detected, suggesting less defect density in sample Ⅱ.

Figure 4(b) displays the evolution of the extracted photon energy as a function of temperature. There is a turning point at 260 K for peak Ⅳ (red plot). Its photon energy exhibits a linear redshift from room temperature to 260 K, then a non-linear

blue-shift from 26 K to 120 K. It is obviously different from that of sample Ⅲ and previous results.[9,12,21] Below 120 K, a new peak appears at 1.72 eV (peak V, blue plot), which belongs to the orthorhombic phase $MAPbI_3$. More details about the peak fitting are shown in Fig. S5. For comparison, temperature-dependent PL measurements were carried out on region B in sample Ⅱ (black plot). The evolution of the main peak's photon energy coincides with that in region A except for that in the range from 300 K to 260 K (peak VI). It is well-known that the photon energy evolution as a function of temperature in either single crystalline bulk or thin films[45] keeps a linear redshift in the stable tetragonal phase and a second-order phase transition from tetragonal to orthorhombic occurs at low temperature.[46] Moreover, $MAPbI_3$ nanocrystals with a size less than 8 nm have no apparent phase transition even at a temperature as low as 80 K.[12] Although $MAPbI_3$ on sapphire in sample Ⅱ is nanocrystals, their sizes are significantly larger, close to those in the thin-film phase. The different photon energy evolutions in sample Ⅱ may show a special crystal/electronic-structure relationship. A similar trend to that of $MAPbI_3$ on $MoS_2$ is observed in $MA_xFA_{1-x}PbI_3$ films accompanied by a different phase transition,[45] where a turning point in the photon energy evolution is attributed to the occurrence of a second-order transition from cubic to tetragonal phase. Here, $MAPbI_3$ was co-deposited on the monolayer $MoS_2$ and growing in van der Waals epitaxy, forming a clean and molecular sharp interface. We propose that $MAPbI_3$ in cubic phase may be formed at room temperature on $MoS_2$ and a second-order phase transition from cubic to another different tetragonal phase occurs at 260 K, called tetragonal-Ⅱ. Below 120 K, a transition from tetragonal-Ⅱ to the orthorhombic phase starts to take place. For $MAPbI_3$ on sapphire, one phase transition from tetragonal-Ⅱ to orthorhombic starts to take place at 100 K. The atomic mode of tetragonal-Ⅱ phase belonging to the $I4cm$ space group is shown in the inset of Fig. 4(a),[47] where the disordered organic cations may rotate in increments along the $c$-axis and affect the tilting of the corner-shared $PbI_6$ octahedron. Moreover, the tilting increases with the temperature decreasing. It gives rise to an opposite effect to the electron-phonon coupling induced gap renormalization, leading to the non-monotonic change of the photon energy.[48]

Figure 4(c) shows the evolution of the extracted FWHM of peak IV with temperature. The broadening behaviors can be described by the one-oscillator model of the electron–phonon interaction:[49]

$$\Gamma(T) = \Gamma_0 + \sigma T + \frac{\Gamma_{\rm op}}{\exp(\hbar w_{\rm op}/K_{\rm B}T) - 1}.$$

Here, $\Gamma_0$ is the inhomogeneous broadening contribution depending on the crystal quality, which is a constant and does not change with temperature; $\sigma$ and $\Gamma_{\rm op}$ are the exciton-acoustic phonon interaction and the exciton-optical phonon contribution to the FWHM broadening; $\hbar\omega_{\rm op}$ is the efficient optical-phonon energy, corresponding to the torsion mode of the organic cations.[45,50] Due to the main emission peak belonging to the free-exciton recombination, $\sigma = 0$ is reasonable for ignoring the acoustic-phonon contribution. In the best fitting, the parameters are $\Gamma_0 = 30.0 \pm 2.3$ meV, $\Gamma_{\rm op} = 144.7 \pm 7.5$ meV, and $\hbar\omega_{\rm op} = 25.1 \pm 5.0$ meV, in agreement with the previous report.[21] Molecularly thin film of $MAPbI_3$ prepared by co-deposition on monolayer $MoS_2$ has better crystalline and novel exciton behavior, which could be beneficial for getting atomically clean interfaces and investigating related properties.

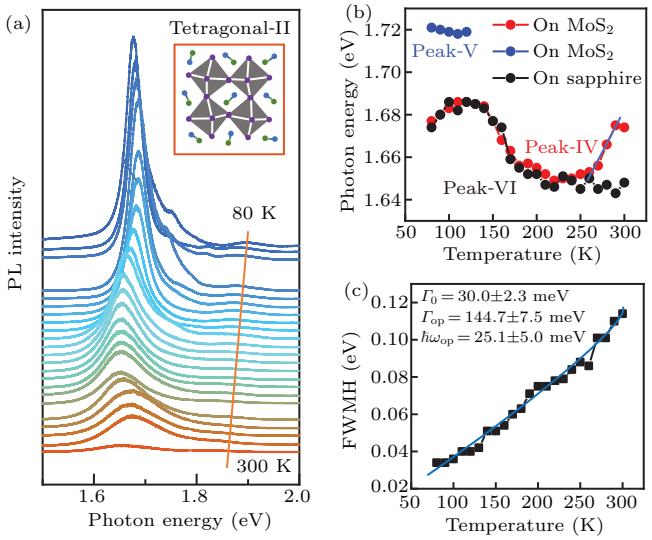



**Fig. 4.** Optical transition properties of sample Ⅱ in the temperature range of 300–80 K. (a) Temperature-dependent PL spectra. Inset: atomic model of tetragonal-Ⅱ phase. (b) Experimental data of photon energy of $MAPbI_3/MoS_2$ (red: tetragonal phase, blue: orthorhombic phase) and pure $MAPbI_3$ (black). (c) Experimental data (black) and fitting curve (blue) of FWHM of tetragonal phase as a function of temperature on $MAPbI_3/MoS_2$ heterostructure.

## 4. Conclusion

In summary, while $MAPbI_3$ grows in a Volmer–Weber mode on sapphire, it can appear in a Stranski–Krastanov mode on single layer $MoS_2$, which gives an opportunity to prepare molecularly thin $MAPbI_3/MoS_2$ heterojunction. Such heterojunctions have a type-Ⅱ energy level alignment and are good candidates for optoelectronic devices. Temperature-dependent PL measurements reveal that such molecularly thin $MAPbI_3$ has a different emission property compared with thin films of either nanocrystals or bigger grains. The second-order phase transitions are observed at 120 K and 150 K. Our research creates more potential to fabricate molecularly thin heterostructures and provides a platform to study novel applications.

## Acknowledgements

Project supported by the National Natural Science Foundation of China (Grant Nos. 11874427 and 11804395) and the

Fundamental Research Funds for the Central Universities of Central South University (Grant No. 2020zzts377).

## References


[1] Dou L, Wong Andrew B, Yu Y, Lai M, Kornienko N, Eaton Samuel W, Fu A, Bischak Connor G, Ma J, Ding T, Ginsberg Naomi S, Wang L-W, Alivisatos A P and Yang P 2015 *Science* **349** 1518

[2] Yang S, Chen S, Mosconi E, Fang Y, Xiao X, Wang C, Zhou Y, Yu Z, Zhao J, Gao Y, De Angelis F and Huang J 2019 *Science* **365** 473

[3] Zhong Y, Liao K, Du W, Zhu J, Shang Q, Zhou F, Wu X, Sui X, Shi J, Yue S, Wang Q, Zhang Y, Zhang Q, Hu X and Liu X 2020 *ACS Nano* **14** 15605

[4] Dong J, Xu X, Shi J J, Li D M, Luo Y H, Meng Q B and Chen Q 2015 *Chin. Phys. Lett.* **32** 078401

[5] Du X, Chen S, Lin D X, Xie F Y, Chen J, Xie W G and Liu P Y 2018 *Acta Phys. Sin.* **67** 098801 (in Chinese)

[6] Kojima A, Teshima K, Shirai Y and Miyasaka T 2009 *J. Am. Chem. Soc.* **131** 6050

[7] Stranks Samuel D, Eperon Giles E, Grancini G, Menelaou C, Alcocer Marcelo J P, Leijtens T, Herz Laura M, Petrozza A and Snaith Henry J 2013 *Science* **342** 341

[8] Sun X G, Shi Z F, Li Y, Lei L Z, Li S, Wu D, Xu T T, Tian Y T and Li X J 2017 *J. Alloys Compd.* **706** 274

[9] Wu K, Bera A, Ma C, Du Y, Yang Y, Li L and Wu T 2014 *Phys. Chem. Chem. Phys.* **16** 22476

[10] Even J, Pedesseau L and Katan C 2014 *J. Phys. Chem. C* **118** 11566

[11] Wehrenfennig C, Liu M, Snaith H J, Johnston M B and Herz L M 2014 *J. Phys. Chem. Lett.* **5** 1300

[12] Rubino A, Francisco-Lopez A, Barker A J, Petrozza A, Calvo M E, Goni A R and Miguez H 2021 *J. Phys. Chem. Lett.* **12** 569

[13] Mirzehmet A, Ohtsuka T, Abd Rahman S A, Yuyama T, Kruger P and Yoshida H 2021 *Adv. Mater.* **33** 2004981

[14] Rubino A, Anaya M, Galisteo-López J F, Rojas T C, Calvo M E and Míguez H 2018 *ACS Appl. Mater. Interfaces* **10** 38334

[15] Liu J, Xue Y, Wang Z, Xu Z Q, Zheng C, Weber B, Song J, Wang Y, Lu Y, Zhang Y and Bao Q 2016 *ACS Nano* **10** 3536

[16] Tang G, You P, Tai Q, Yang A, Cao J, Zheng F, Zhou Z, Zhao J, Chan P K L and Yan F 2019 *Adv. Mater.* **31** 1807689

[17] Liu Z, Liu K, Zhang F, Jain S M, He T, Jiang Y, Liu P, Yang J, Liu H and Yuan M 2020 *Sol. Energy* **195** 436

[18] Li Z, Li J, Ding D, Yao H, Liu L, Gong X, Tian B, Li H, Su C and Shi Y 2018 *ACS Appl. Mater. Interfaces* **10** 36493

[19] Yu Y, Miao F, He J and Ni Z 2017 *Chin. Phys. B* **26** 036801

[20] Yang T, Wang X, Zheng B, *et al.* 2019 *ACS Nano* **13** 7996

[21] Shao Z, Xiao J, Guo X, You S, Zhang Y, Li M, Song F, Zhou C, Xie H, Gao Y, Sun J and Huang H 2022 *Curr. Appl. Phys.* **36** 27

[22] Shao Z, You S, Guo X, Xiao J, Liu J, Song F, Xie H, Sun J and Huang H 2022 *Results Phys.* **34** 105326

[23] Liu M, Johnston M B and Snaith H J 2013 *Nature* **501** 395

[24] Ono L K, Wang S, Kato Y, Raga S R and Qi Y 2014 *Energy Environ. Sci.* **7** 3989

[25] Liu S and MandHan W Z 2019 *Acta Phys. Sin.* **68** 137901 (in Chinese)

[26] Shi J, Wu D, Zheng X, Xie D, Song F, Zhang X, Jiang J, Yuan X, Gao Y and Huang H 2018 *Phys. Status Solidi B* **255** 1800254

[27] Deng R, Zhang H, Zhang Y, Chen Z, Sui Y, Ge X, Liang Y, Hu S, Yu G and Jiang D 2017 *Chin. Phys. B* **26** 067901

[28] Tian Q, He B, Zhao Y, Wang S, Xiao J, Song F, Wang Y, Lu Y, Xie H, Huang H and Gao Y 2019 *Synth. Met.* **251** 24

[29] Wu D, Yang Y, Zhu P, Zheng X, Chen X, Shi J, Song F, Gao X, Zhang X, Ouyang F, Xiong X, Gao Y and Huang H 2018 *J. Phys. Chem. C* **122** 1860

[30] Liu J, Sun K, Zheng X, Wang S, Lian S, Deng C, Xie H, Zhang X, Gao Y, Song F and Huang H 2020 *Results Phys.* **19** 103634

[31] Guo X, Tian Q, Wang Y, Liu J, Jia G, Dou W, Song F, Zhang L, Qin Z and Huang H 2022 *Carbon* **190** 312

[32] Dumcenco D, Ovchinnikov D, Marinov K, Lazić P, Gibertini M, Marzari N, Sanchez O L, Kung Y C, Krasnozhon D, Chen M W, Bertolazzi S, Gillet P, Fontcuberta I Morral A, Radenovic A and Kis A 2015 *ACS Nano* **9** 4611

[33] Gidey A T, Assayehegn E and Kim J Y 2021 *ACS Appl. Energy Mater.* **4** 6923

[34] Li Y, Xu X, Wang C, Wang C, Xie F, Yang J and Gao Y 2015 *AIP Adv.* **5** 097111

[35] Zhang K, Zhang T, Cheng G, *et al.* 2016 *ACS Nano* **10** 3852

[36] Gallet T, Poeira R G, Lanzoni E M, Abzieher T, Paetzold U W and Redinger A 2021 *ACS. Appl. Mater. Interfaces* **13** 2642

[37] Taurisano N, Bravetti G, Carallo S, Liang M, Ronan O, Spurling D, Coelho J, Nicolosi V, Colella S, Gigli G, Listorti A and Rizzo A 2021 *Nanomaterials* **11** 1706

[38] Sun Y, Yin Y, Pols M, *et al.* 2020 *Adv. Mater.* **32** 2002392

[39] Kronik LandKummel S 2018 *Adv. Mater.* **30** 1706560

[40] Niu L, Liu X, Cong C, *et al.* 2015 *Adv. Mater.* **27** 7800

[41] Shi Z F, Li Y, Li S, Ji H F, Lei L Z, Wu D, Xu T T, Xu J M, Tian Y T and Li X J 2017 *J. Mater. Chem. C* **5** 8699

[42] Leguy A M, Goni A R, Frost J M, Skelton J, Brivio F, Rodriguez-Martinez X, Weber O J, Pallipurath A, Alonso M I, Campoy-Quiles M, Weller M T, Nelson J, Walsh A and Barnes P R 2016 *Phys. Chem. Chem. Phys.* **18** 27051

[43] Wu X, Trinh M T, Niesner D, Zhu H, Norman Z, Owen J S, Yaffe O, Kudisch B J and Zhu X Y 2015 *J. Am. Chem. Soc.* **137** 2089

[44] O'Donnell K P and Chen X 1991 *Appl. Phys. Lett.* **58** 2924

[45] Francisco-López A, Charles B, Alonso M I, Garriga M, Campoy-Quiles M, Weller M T and Goñi A R 2020 *J. Phys. Chem. C* **124** 3448

[46] Francisco-Lopez A, Charles B, Weber O J, Alonso M I, Garriga M, Campoy-Quiles M, Weller M T and Goni A R 2019 *J. Phys. Chem. Lett.* **10** 2971

[47] Stoumpos C C, Malliakas C D and Kanatzidis M G 2013 *Inorg. Chem.* **52** 9019

[48] Ghosh D, Walsh Atkins P, Islam M S, Walker A B and Eames C 2017 *ACS Energy Lett.* **2** 2424

[49] Rudin S, Reinecke T L and Segall B 1990 *Phys. Rev. B* **42** 11218

[50] Quarti C, Grancini G, Mosconi E, Bruno P, Ball J M, Lee M M, Snaith H J, Petrozza A and Angelis F D 2014 *J. Phys. Chem. Lett.* **5** 279